



## OPEN

# Fabrication of thickness controllable free-standing sandwich-structured hybrid carbon film for high-rate and high-power supercapacitor

SUBJECT AREAS:  
POROUS MATERIALS  
ELECTRONIC PROPERTIES AND  
DEVICES

Received  
28 July 2014

Accepted  
22 October 2014

Published  
14 November 2014

Correspondence and  
requests for materials  
should be addressed to  
H.L.W. (hlwei@hust.  
edu.cn)

Helin Wei<sup>1</sup>, Sihang Wei<sup>2</sup>, Weifeng Tian<sup>1</sup>, Daming Zhu<sup>1</sup>, Yuhao Liu<sup>1</sup>, LiliYuan<sup>1</sup> & Xin Li<sup>1</sup>

<sup>1</sup>School of Physics, Huazhong University of Science and Technology, Wuhan, Hubei, 430074, PR China, <sup>2</sup>State Key Laboratory for Superlattices and Microstructures, Institute of Semiconductors, Chinese Academy of Sciences, P.O. Box 912, Beijing 100083, PR China.

Hybrid carbon films composed of graphene film and porous carbon film may give full play to the advantages of both carbon materials, and have great potential for application in energy storage and conversion devices. Unfortunately, there are very few reports on fabrication of hybrid carbon films. Here we demonstrate a simple approach to fabricate free-standing sandwich-structured hybrid carbon film composed of porous amorphous carbon film and multilayer graphene film by chemical vapor deposition in a controllable and scalable way. Hybrid carbon films reveal good electrical conductivity, excellent flexibility, and good compatibility with substrate. Supercapacitors assembled by hybrid carbon films exhibit ultrahigh rate capability, wide frequency range, good capacitance performance, and high-power density. Moreover, this approach may provide a general path for fabrication of hybrid carbon materials with different structures by using different metals with high carbon solubility, and greatly expands the application scope of carbon materials.

**D**esign and preparation of carbon materials with appropriate structures and physical/chemical properties matching the requirements of their applications are extremely important. Carbon materials with a 2-dimensional (2D) uniform structure may be more beneficial in applications related to energy storage and separation/filtration processes. Graphene, a typical 2D structure, has immense strength, high aspect ratio and extremely high electrical conductivity<sup>1,2</sup>. Porous amorphous carbon film (PACF) has high specific surface area and abundant porous structure<sup>3,4</sup>. Therefore, graphene and PACF are currently the most commonly applied electrodes for energy storage devices, and notable progresses have been achieved<sup>3–11</sup>. However, restack, easily broken and agglomerate in application process severely suppress intrinsic properties of graphene<sup>6,12,13</sup>. Poor electrical conductivity, complex fabrication process<sup>3,9,10</sup> and sometime binder-used<sup>4,14</sup> significantly affect the stability and repeatability of PACF-based devices. Hybrid carbon film (HCF) composed of graphene and porous carbon material may overcome the above mentioned shortcomings and give full play to the advantages inherited from both carbon materials. For example, HCFs show good adhesion, electrically conductive, and mechanical property<sup>15–17</sup>, as well as high reversible capacity with excellent cyclic stability<sup>18,19</sup> and high hydrogen storage capacity<sup>20</sup>. Regrettably, there are only a few reports on fabricating HCFs in an uncontrollable way<sup>15–20</sup>. In addition, these methods are not suitable for fabrication of free-standing HCFs. The successful synthesis of free-standing HCFs will provide many unique advantages for their applications (such as electrode materials), including: (i) 2D structure easily matching with electrode shape, (ii) small volume effectively improving utilization of material and facilitating charge transport, and (iii) easy transfer and binder-free beneficial to optimize device performance.

Chemical vapor deposition (CVD), a simple and easy controlling technique, is often used to fabricate large-area graphene<sup>21–25</sup>. Recently, ultrathin amorphous carbon film<sup>26</sup> and HCFs composed of graphene (nanowhiskers/film) and amorphous carbon (ultrathin-film/ball)<sup>17,27</sup> can be fabricated on Cu foil or Ni foil by CVD. However, the structure and thickness of the HCF prepared by CVD are not controllable. Ni foil is commonly applied catalytic metal for growth of large-area multilayer graphene film (MGF) because of its higher carbon solubility and diffusivity<sup>28</sup>. During CVD growth of graphene on Ni foil, carbon atoms undergo two processes: dissolution and segregation/precipitation<sup>23,24,28–31</sup>. It's worth noting that not all the carbon atoms can segregate/precipitate



onto Ni surface to form graphene, in theory, some of dissolved carbon atoms may remain in Ni foil after graphene growth. We recently found that a large number of dissolved carbon atoms can be trapped in Ni foil during CVD process by controlling experimental conditions.

Inspired by the above fact, we herein report a new approach to fabricate large-area free-standing sandwich-structured HCF composed of MGF and PACF by ambient pressure CVD (APCVD). The thickness of the HCF can be controlled by experimental conditions. Our HCF can be easily transferred to arbitrary substrates of interest, and has high conductivity, excellent flexibility, and good compatibility with substrate. Binder-free supercapacitor based on HCF (1.12  $\mu\text{m}$  thick) exhibits a high rate capability, wide frequency range for capacitive feature, superior cycling stability, and good capacitance performance with area specific capacitance of 0.48  $\text{mF}/\text{cm}^2$ . Furthermore, the HCF-based supercapacitor shows a high power density with maximum power density of 3.00  $\text{kW}/\text{kg}$  (1.49  $\text{W}/\text{cm}^3$ ). The capacitance and power density of the HCF-based supercapacitor are further improved to 1.08  $\text{mF}/\text{cm}^2$  and 6.20  $\text{kW}/\text{kg}$  (3.10  $\text{W}/\text{cm}^3$ ) as the HCF thickness is increased to 1.83  $\mu\text{m}$ . This new method is simple, controllable, and scalable to industrial levels.

## Results

**Design and fabrication of free-standing HCF.** Figure 1 illustrates a schematic representation of the fabrication process of free-standing HCF. After methane decomposition at growth temperature, carbon atoms adsorb on Ni surface, and then diffuse and dissolve in Ni foil (Figure 1a). Over time, a large number of carbon atoms dissolve in Ni foil because of higher carbon solubility and diffusivity of the Ni metal<sup>28–31</sup>, and graphene grows on Ni surface at the same time (Figure 1b). It is generally believed that the dissolved carbon atoms segregate/precipitate on Ni surface to form MGF during rapid cooling process<sup>28–31</sup>. However, it should be noted that this segregation/precipitation process may be limited by: (1) rapidly cooling which may result in a quench effect in which the dissolved carbon atoms lose the mobility<sup>23,28,31</sup>; and (2) high work pressure and high concentration of carbon atom which may hinder the segregation/

precipitation of the dissolved carbon atoms during APCVD process. As a result, only part of the dissolved carbon atoms can segregate/precipitate on the Ni surface to form MGF, and a large number of carbon atoms will be trapped in Ni foil (Figure 1c). After APCVD growth, the Ni foil is immersed in a ferric chloride solution, and the MGF is detached from the Ni foil in a short time (Figure 1d). Free-standing sandwich-structured HCF (MGF/PACF/MGF) can be obtained as the Ni foil is completely etched (Figure 1e). On the other hand, after the removal of the MGFs, free-standing PACF forms as the Ni foil is completely etched (Figure 1f–1i). The formation process of the PACF can be described as following: first, Ni atoms dissolve in ferric chloride solution (Figure 1f) and carbon atoms appear on the surface of the Ni foil; then, carbon atoms connect with each other to form carbon particles (Figure 1g) and carbon film (Figure 1h). During corrosion process, carbon atom bonds fairly readily with other carbon atoms, rather than Ni atoms, this is because bond energy of C–C (347.3  $\text{kJ}/\text{mol}$ ) is larger than that of Ni–C (147  $\text{kJ}/\text{mol}$ ). In other words, C–C bond is more stable. Finally, a layer of PACF forms (Figure 1i).

The fabrication process of HCF is continuously recorded by a digital camera, as shown in Figure 2. Pure Ni foil has a smooth surface with silver-grey color before APCVD growth (Figure 2a), and becomes dark-grey color after APCVD growth (Figure 2b) (experimental condition: flow ratio of  $\text{CH}_4 : \text{H}_2 = 80 : 8$ , and growth temperature of  $900^\circ\text{C}$ ), implying MGF grows on the surface of Ni foil. Then, the Ni foil is immersed into ferric chloride solution. After two minutes, the MGFs are detached from two surfaces of the Ni foil. Gently lifting the Ni foil to the solution surface and then putting it down, the MGF automatically departs and floats on the solution surface (Figure 2c). After 5 hours, a layer of PACF forms inbetween two MGFs as the Ni atoms are completely dissolved (Figure 2d). If the Ni foil is not touched/moved during corrosion process, a sandwich-structured HCF (MGF/PACF/MGF) can be obtained (Figure 2e). Three-layer structure can be clearly seen from the inset in Figure 2e. To clearly show the formation process of the PACF, after the removal of the MGFs, the Ni foil (Figure 2f) is put into ferric

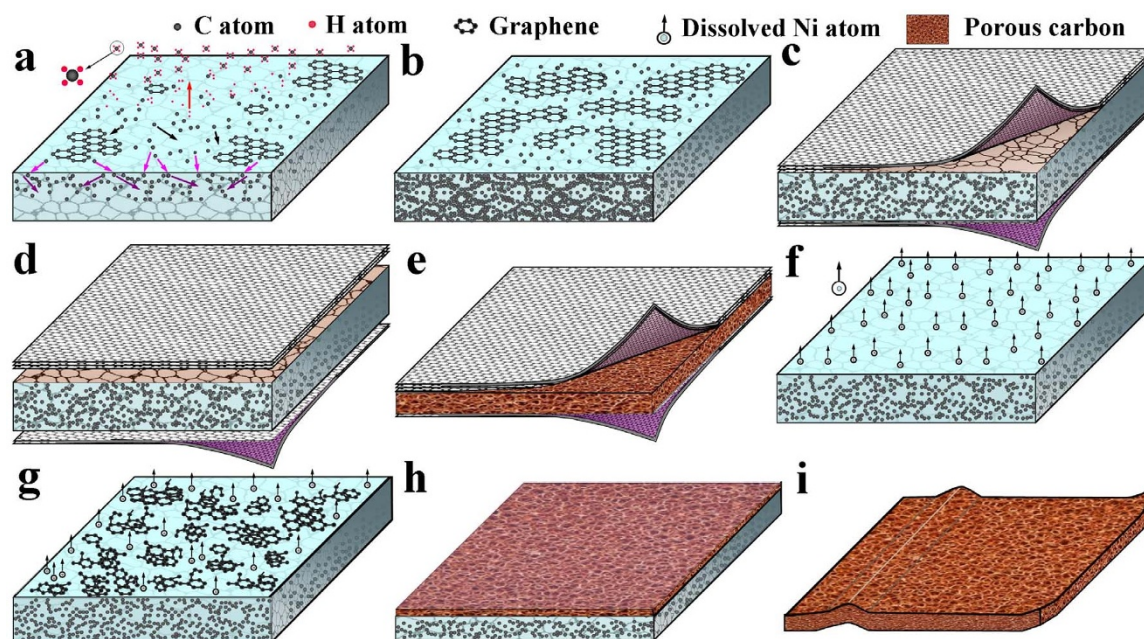


**Figure 1 | Design of free-standing carbon films.** Schematic illustration of the fabrication process of HCF and PACF, (a) decomposition of methane, carbon atom adsorption, diffusion and dissolution at growth temperature, (b) graphene growing and a large number of carbon atoms dissolving in Ni foil, (c) part of the carbon atoms segregating/precipitating on Ni surface to form MGF, and another part of the carbon atoms trapped in Ni foil, (d) MGFs detaching from both sides of the Ni foil in ferric chloride solution, (e) free-standing HCF after Ni foil completely etched, (f) etching Ni foil in ferric chloride solution after the removal of MGFs, (g) and (h) etching Ni foil and formation of the PACF, (i) free-standing PACF after Ni foil completely etched.

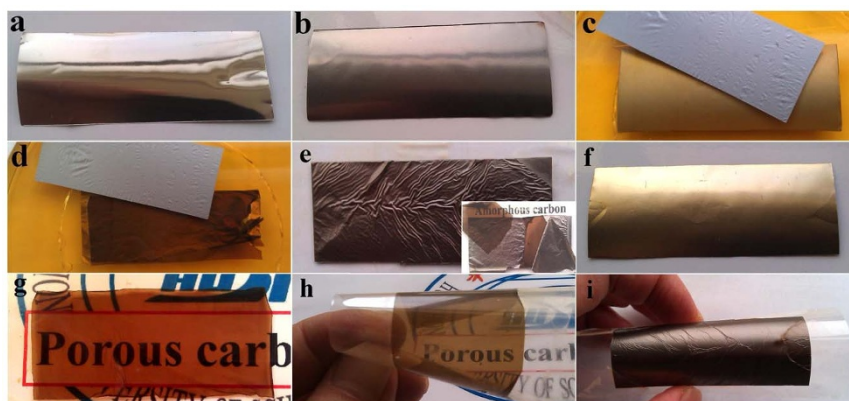


**Figure 2 | Fabrication process of free-standing carbon films.** Photographic images of (a) pure Ni foil before APCVD growth, (b) Ni foil after MGF APCVD growth, (c) Two minutes later, MGFs detaching from Ni foil in ferric chloride solution, (d) MGFs and PACF after Ni foil completely etched, (e) free-standing HCF (inset shows the three-layer hybrid structure –MGF/PACF/MGF), (f) Ni foil after the removal of MGFs, (g) PACF after Ni foil completely etched, (h) PACF and (i) HCF on flexible plastic sheets.

chloride solution. After about 5 hours, a layer of transparent film with brown color forms (Figure 2g). Obviously, this transparent film is carbon film, and the transparent characteristic implies that the carbon film has a porous structure. The area of the carbon film is about  $5.4 \times 2.4 \text{ cm}^2$ , which is smaller than that of the Ni foil ( $7.0 \times 3.0 \text{ cm}^2$ ). The HCF (including MGF and PACF) can be directly transferred to arbitrary substrates for characterization and application. Figure 2h and 2i show the PACF and HCF on a plastic sheet, which reveal excellent flexibility and good compatibility with the substrate.

Surface topographies of the Ni foil at the initial stage of corrosion process are investigated by metallographic microscope, and shown in Figure 3. Figure 3a shows the surface topography of pure Ni foil before APCVD growth, which is gray and shows pronounced striations. Immersing the Ni foil into ferric chloride solution, the striation lines are still clearly shown after 5 minutes (Figure 3b), implying the Ni foil is slightly corroded. Noteworthy, part of the surface is covered by a layer of discontinuous film-like structure, which is pale brown yellow (inset in Figure 3b). The surface morphology and elemental composition of the film-like structure are observed by SEM and EDS, and shown in Figure S1 (Supplementary information). The SEM image shows two regions with different colors (dark and gray), and the EDS analysis clearly shows the carbon content in dark region is 35.58%, five times higher than that in gray region (7.12%). This result indicates that the film-like structure is carbon film. With the increase in corrosion time, the surface is almost covered by the carbon film,

which becomes brown (Figure 3c and inset). It is interesting to note that the carbon film close to the grain boundaries of Ni foil becomes light blue color (inset in Figure 3c). Further increasing corrosion time, the surface is totally covered by carbon film (Figure 3d). The area of the blue region gradually increases, and the color becomes gradually from light blue to dark blue, and then to dark purple (Figure 3d–f), implying the increase of the carbon film thickness.

**Microstructure and property of the HCF.** The crystal structures of the MGF and PACF are firstly investigated by x-ray diffraction (XRD), and as shown in Figure S2. Figure S2a illustrates the XRD pattern of as-grown carbon film on Ni foil. The diffraction peaks at  $44.4^\circ$ ,  $51.6^\circ$  and  $76.4^\circ$  are reflections of the Ni foil. The sharp diffraction peak at  $26.6^\circ$  and the broad diffraction peak at  $21.9^\circ$  belong to the diffraction peaks of the carbon films (Figure S2b and S2c). From the XRD pattern of the MGF (Figure S2b), the spacing obtained from Bragg equation is 0.336 nm for the diffraction peak at  $26.6^\circ$ , which is corresponding to graphite. The broadening peak at  $21.9^\circ$  is due to short-range order of the graphene sheets along the stacking direction. From the XRD pattern of the PACF (Figure S2c), only one broadening peak at  $22.5^\circ$  can be observed. This broadening of the diffraction peak implies that the carbon film has amorphous characteristic.

Microstructures and morphologies of the MGF and PACF are investigated by TEM, SEM and Raman spectroscopy. Figure 4a shows a SEM image of the MGF transferred on Si substrate. The

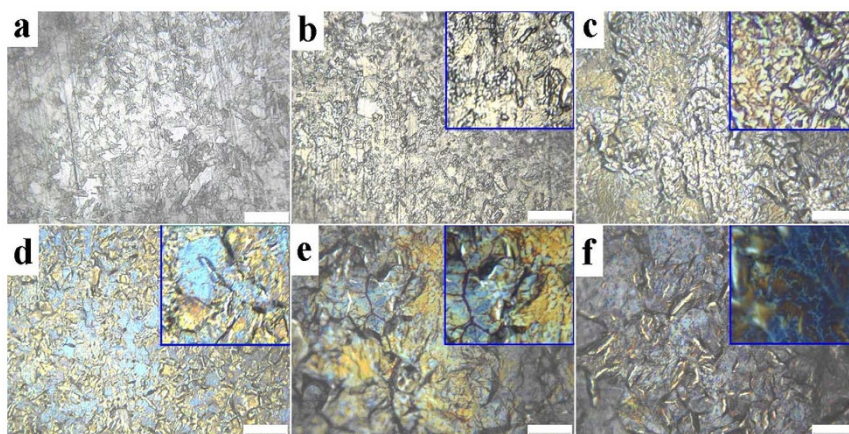


**Figure 3 | Metallographic microscope topographies of Ni foil surface.** (a) Pure Ni foil. Ni foil is corroded in ferric chloride solution after (b) 5 minutes, (c) 10 minutes, (d) 20 minutes, (e) 30 minutes, and (f) 40 minutes. Insets are enlarged microscope topographies. The scale bar represents 20  $\mu\text{m}$ .

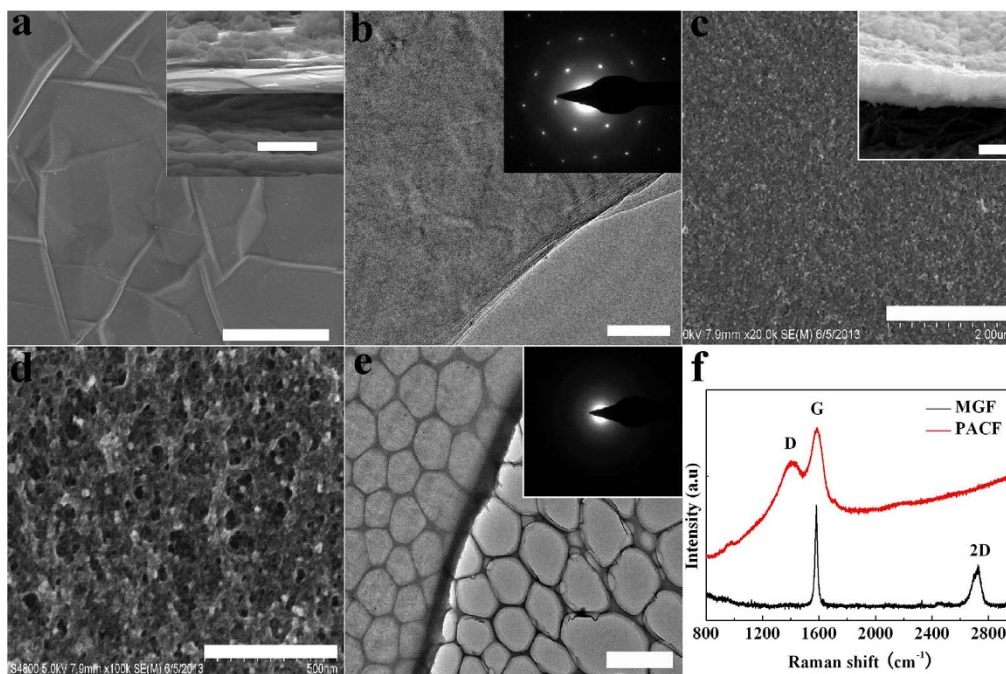


**Figure 4** | The microstructures of the MGF and PACF in HCF. (a) SEM image of MGF (scale bar represents 4  $\mu\text{m}$ ), inset shows the cross-sectional SEM image of the MGF, scale bar represents 1  $\mu\text{m}$ , (b) TEM image of MGF, the scale bar represents 50 nm, inset shows the SAED pattern, (c) SEM image of PACF, the scale bar represents 2  $\mu\text{m}$ , inset shows the cross-sectional SEM image of the PACF, scale bar represents 1  $\mu\text{m}$ , (d) high magnification SEM image of PACF, the scale bar represents 500 nm, (e) TEM image of PACF, the scale bar represents 2  $\mu\text{m}$ , inset is the SAED pattern, and (f) Raman spectra of MGF and PACF.

thickness of the MGF is about 60 nm from the cross sectional SEM image (inset in Figure 4a). High magnification TEM image and SAED pattern of the MGF are shown in Figure 4b. The SAED pattern (inset in Figure 4b) shows a typical hexagonal symmetry pattern, which is representative for graphene layers. Figure 4c shows a typical SEM image of the PACF. The SEM image shows that the PACF is uniform and continuous. The thickness is about 1.00  $\mu\text{m}$  from the cross sectional SEM image (inset in Figure 4c). High magnification SEM image shows the PACF has a porous-like structure (Figure 4d). It is interesting to note that the PACF has a very broad pore size distribution, which is beneficial for its application required in supercapacitors. The TEM image (Figure 4e) and the SAED pattern (inset in Figure 4e) further confirm the PACF has a uniform and amorphous structure.

The Raman spectra of the MGF and PACF are shown in Figure 4f. The in-plane vibration related G-peak ( $1583\text{ cm}^{-1}$ ) and second-order process related 2D-peak ( $2712\text{ cm}^{-1}$ ) can be clearly observed from the Raman spectrum of MGF. The absence of D peak (disorder/defects band) at about  $1360\text{ cm}^{-1}$  implies that the MGF is well-ordered. The FWHM of the 2D peak is  $56\text{ cm}^{-1}$ , and the intensity ratio of  $I_{2D}/I_G$  is about 0.46, indicating the graphene film is multilayer<sup>32</sup>. Raman spectrum of the PACF shows two sharp peaks at  $1407\text{ cm}^{-1}$  and  $1581\text{ cm}^{-1}$ , assignable to the D and G band<sup>32</sup>, respectively. The broadening of the D and G peaks is characteristics of amorphous nature of PACF duo to the short-range order<sup>33</sup>. Considering the G-peak position ( $1581\text{ cm}^{-1}$ ) and  $I_D/I_G$  ratio (0.60), the PACF is completely disordered according to Ferrari's three-stage mode<sup>33</sup>, which is consistent with the TEM and XRD investigations.

The thicknesses of the MGF and PACF are measured by cross sectional SEM images, and the thicknesses of thin MGF ( $<10\text{ nm}$ ) are estimated from the SEM and TEM images. The effect of the growth temperature and flow ratio ( $\text{CH}_4:\text{H}_2$ ) on the carbon film thickness is shown in Figure 5a. It is clear that the carbon film thicknesses increase with increasing the growth temperature. At high carbon source concentration ( $\text{CH}_4:\text{H}_2 = 80:8\text{ sccm}$ ), the PACF

thickness increases significantly at high temperature zone compared with that at low temperature zone. This is because that the solubility of carbon atoms in Ni increases exponentially with increasing the growth temperature<sup>28–31</sup>. The thickness of the PACF increases from 90 to 1000 nm as the growth temperature increases from 500 to  $900^\circ\text{C}$ . It should be pointed out that continuous PACF can not be obtained as the growth temperature is lower than  $500^\circ\text{C}$  because of the extremely low solubility of carbon atom<sup>28–31</sup>. Similar result is also observed for MGF growth, continuous MGF can be obtained only when the growth temperature is greater than  $620^\circ\text{C}$ . The thickness of the MGF increases from about 10 to 60 nm as the growth temperature increases from 620 to  $900^\circ\text{C}$ . At low carbon source concentration ( $\text{CH}_4:\text{H}_2 = 8:80\text{ sccm}$ ), no MGF and PACF form as the growth temperature is lower than  $600^\circ\text{C}$ . Continuous PACF can be obtained when the growth temperature is greater than  $700^\circ\text{C}$ . The thickness of the PACF increases from 125 to 220 nm as the growth temperature increases from 700 to  $900^\circ\text{C}$ . Continuous MGF can be obtained as the growth temperature is greater than  $850^\circ\text{C}$ , and the thickness of the MGF increases from about 5 to 10 nm with increasing the growth temperature from 850 to  $900^\circ\text{C}$ . The above results suggest that the growth temperature and flow ratio ( $\text{CH}_4:\text{H}_2$ ) greatly influence the growth of carbon film during APCVD growth process.

The sheet resistances of the free-standing carbon films are measured by a standard four probe technique, and as shown in Figure 5b. The sheet resistance of the MGF does not change with increasing the thickness (the thickness of MGF is larger than 5 nm in this measurement). The sheet resistance of the PACF is quite large because of its porous structure (see Figure 4d). The sheet resistance decreases from 25 to  $10\text{ M}\Omega\text{ sq}^{-1}$  with increasing the thickness from 200 to 1000 nm. The decrease of sheet resistance is probably because the thicker PACF provides more channels for electron transport. Notably, the sheet resistance of the PACF is greatly improved by forming a hybrid structure with MGF (middle inset in Figure 5b). This is because of the high conductivity of MGF, which plays a short circuit role. The sheet resistance increases from 34 to  $59\text{ K}\Omega\text{ sq}^{-1}$

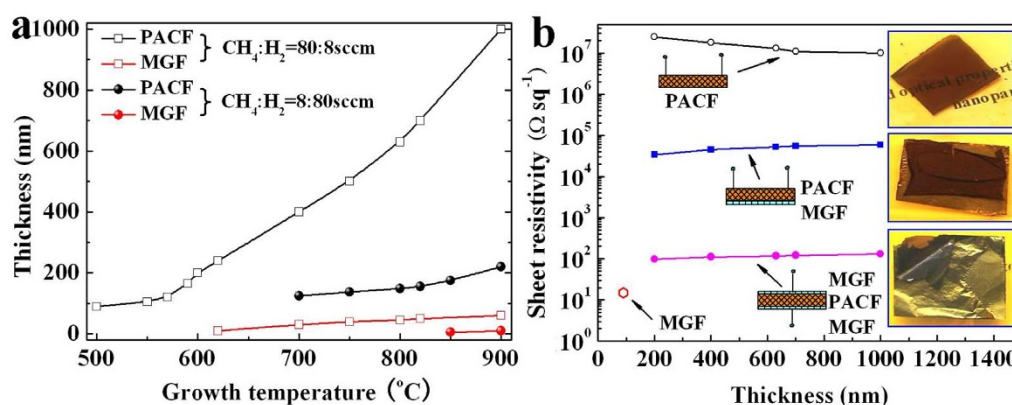


**Figure 5 | Thickness and electrical property of carbon films.** (a) Thickness of the PACF and MGF dependence of growth temperature and methane/hydrogen flow ratio, (b) Sheet resistivity of the carbon films dependence of the thickness of the PACF, insets are the photographic images of the samples.

with increasing the PACF thickness from 200 to 1000 nm. The increase of sheet resistance is probably because the short circuit effect gradually becomes weak as the PACF thickness increases. More interesting, the resistance of sandwich-structured HCF along out-of-plane direction of the HCF (bottom inset in Figure 5b) is very low, and increases from 98 to 131  $\Omega \text{ sq}^{-1}$  with increasing the PACF thickness from 200 to 1000 nm. These results indicate that, either perpendicular or parallel to the direction of film plane, the conductivity can be greatly improved by forming sandwich-structured hybrid structure.

**Supercapacitor based on the HCF.** The above results show that the sandwich-structured HCF has fascinating advantages including porous structure, good conductivity, excellent flexibility, and good compatibility with substrate. Therefore, the sandwich-structured HCF is suitable as an electrode material for supercapacitor (SC). To demonstrate the advantages of the HCF, after being transferred onto a plastic substrate, a binder-free SC is assembled by using a cellulose separator in between two HCFs, in which the HCF serves as both current collector and active material. Two HCF electrodes are fabricated for comparison: i) HCF (1.12  $\mu\text{m}$ ), in which the thicknesses of the MGFs and PACF are about 60 nm and 1.00  $\mu\text{m}$ , respectively, ii) HCF (1.83  $\mu\text{m}$ ), in which the thicknesses of the MGFs and PACF are about 100 nm and 1.63  $\mu\text{m}$ , respectively. The cross sectional SEM images of the MGF and PACF in the HCF (1.83  $\mu\text{m}$ ) are shown in Figure S3. The electrodes and separator are wetted with 6 M KOH aqueous electrolyte for two hours, and then fixed by two clips before testing.

Cyclic voltammograms (CV) curves of the SC based on HCF (1.12  $\mu\text{m}$ ) with increasing scan rate from 100 to 800 mV/s at operating potential between 0.0 and 1.0 V are shown in Figure 6a. The CV curves exhibit nearly rectangular shape, implying virtually pure electrical double-layer capacitive (EDLC) behavior. There is a greatly increase of the current density with increasing the scan rate, which indicates that the HCF-based SC has a small equivalent series resistance (ESR) with rapid ion response and highly capacitive nature. The small ESR comes from the high conductivity of MGF and the low out-of-plane resistance of the sandwich-structured HCF (Figure 5b). The CV curves of the SCs based on different carbon films at scan rate of 50 mV/s at operating potential between 0.0 and 0.8 V are shown in Figure S4a. The area of the CV curve increases greatly with increasing the thickness of the carbon film, indicating the thicker carbon film significantly enhances the capacitance performance. The area specific capacitances ( $C_s$ ) of the HCF electrodes are calculated based on the CV curve, as shown in Figure 6b. The  $C$  of the HCF (1.12  $\mu\text{m}$ ) electrode reaches 0.48  $\text{mF/cm}^2$  at scan rate of 50 mV/cm<sup>2</sup>, which is larger than the area specific capacitances of the multilayer graphene sheets (0.39 and 0.28  $\text{mF/cm}^2$ )<sup>5,34</sup>. It is worth noting that the HCF

electrode is in a three-layer structure, wherein an upper layer and a lower layer are MGFs, and a middle layer is PACF. The electrochemical test shows that the  $C_s$  of the PACF and MGF on Ni foil are about 0.23 and 0.26  $\text{mF/cm}^2$  at scan rate of 50 mV/s (Figure S4b), respectively. The  $C$  of the MGF (0.26  $\text{mF/cm}^2$ ) is close to that of the multilayer graphene sheet (0.28  $\text{mF/cm}^2$ )<sup>34</sup>. Increasing the thickness of the HCF, the performance of the SC can be significantly improved. The  $C$  of the HCF (1.83  $\mu\text{m}$ ) electrode reaches 1.08  $\text{mF/cm}^2$ , increasing more than two times compared with that of the HCF (1.12  $\mu\text{m}$ ) electrode (Figure 6b). When the scan rate increases from 50 to 1000 mV/s, the  $C$  of the HCF (1.12  $\mu\text{m}$ ) decreases to 77%, and is decreased by only 23%, which implies that the HCF-based SC possesses an excellent electrochemical stability.

Galvanostatic charge/discharge (GCD) curves of the SC based on HCF (1.12  $\mu\text{m}$ ) at different current densities are shown in Figure 6c. The discharge curves of the SCs based on different carbon films at current density of 0.10  $\text{mA/cm}^2$  are shown in Figure S4c. The GCD curves show a typical triangular shape, and the discharge curves have linear characteristics, indicating nearly ideal capacitive behavior. No obvious IR drops are observed in Figure 6c and Figure S4c, indicating again the HCF-based SCs have low ESR. The electrode is tested for 2000 cycles at a current density of 0.10  $\text{mA/cm}^2$  and shows no visible capacitance loss (Figure 6d), which implies the HCF-based SC has superior cycling stability. The Nyquist plots of the HCF-based SCs are shown in Figure 6e. In high frequency region, the low intercept at Z real axis is related to the ESR of the device, the ESRs are 0.91 and 1.62  $\Omega$  for the SC based on HCF (1.12  $\mu\text{m}$ ) and HCF (1.83  $\mu\text{m}$ ) electrodes, respectively. The plots are characterized by a high-frequency semicircle and then a straight line (inset in Figure 6e). The high-frequency semicircle is generally interpreted as the charge-transport resistance in active materials or the contact resistance at the interface<sup>7</sup>. The transition region between the high-frequency semicircle and the vertical line region has 45° feature, indicating typical Warburg impedance. This result reflects that the HCF has a porous structure<sup>6</sup> as confirmed by SEM image. In low frequency region, the plot manifests itself by a line that intersects the real axis at a near 90° angle, which is consistent with an ideal EDLC behavior<sup>7,35</sup>.

The dependence of phase angle on the frequency from 10<sup>-2</sup> to 10<sup>5</sup> Hz is shown in Figure 6f. The curves show capacitive behavior with phase angle of nearly -90° at low frequency and inductive behavior at high frequency<sup>6</sup>. The HCF-based SCs have a significantly wide frequency range (~kHz) for the capacitive feature. This frequency range is close to that of the graphene nanosheet SC<sup>6,8,36</sup>, and larger than that of the vertically oriented graphene (VOG)-bridged coated nickel-foam SC<sup>7</sup>. The phase angle reaches -45°, which is commonly adopted to evaluate the frequency performance of SC (resistance and reactance of capacitor have equal magnitudes at this

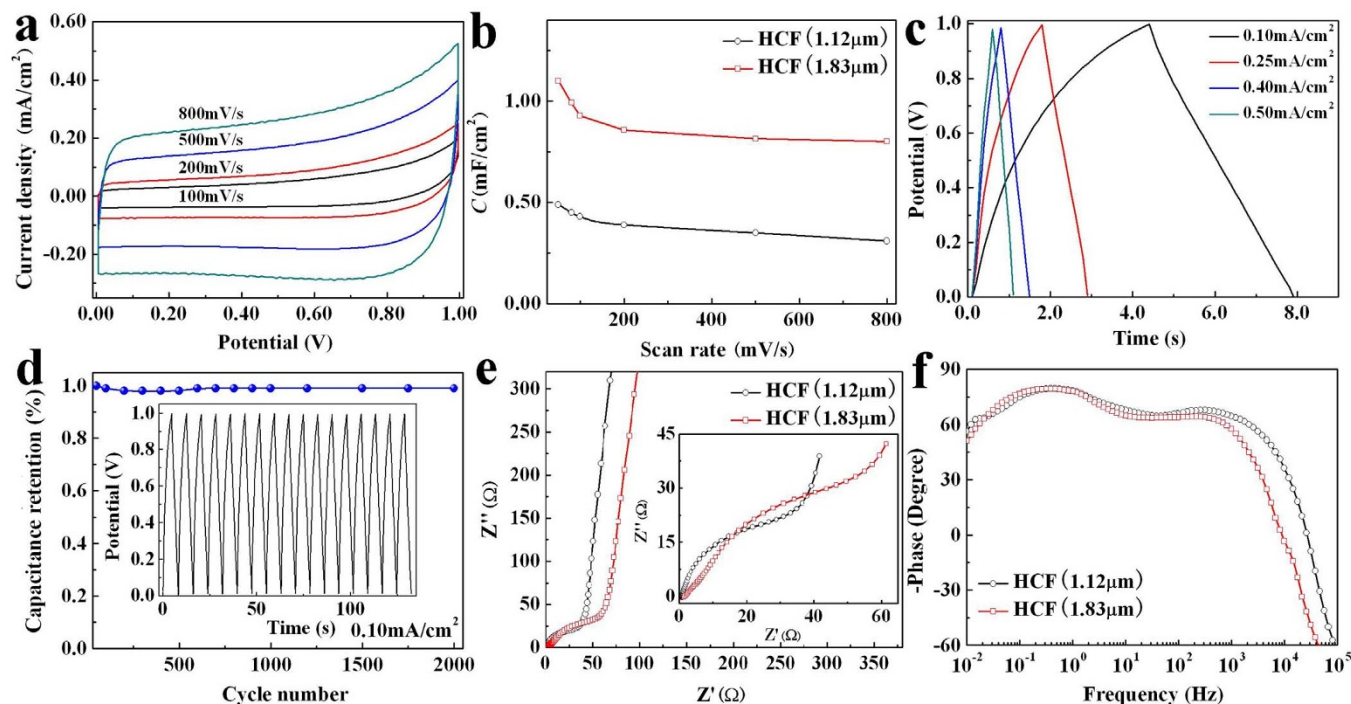


**Figure 6** | Electrochemical performance of HCF-based SC. (a) Cyclic voltammograms (CV) curves of sandwich-structured HCF (1.12  $\mu\text{m}$ ) using a two-electrode symmetrical SC at operating potential between 0.0 and 1.0 V at different scan rates, (b) areal specific capacitance of the HCF electrodes with scan rate, (c) galvanostatic charge/discharge (GCD) curves of the SC based on the HCF (1.12  $\mu\text{m}$ ) at different current densities, (d) cycling stability performance of the SC based on the HCF (1.12  $\mu\text{m}$ ), inset shows the last dozen GCD curves after 2000 cycles at constant current density of 0.10  $\text{mA}/\text{cm}^2$ , (e) Nyquist plots of the HCF-based SCs, and inset shows the magnified portion of the Nyquist plots near the origin, (f) impedance phase angle versus frequency.

frequency), at  $f \approx 7$  kHz for the SC based on the HCF (1.12  $\mu\text{m}$ ). This frequency is much higher than that of the activated carbon SC (0.15  $\text{Hz}$ <sup>6</sup>), the vertically oriented graphene SC ( $\sim 9$   $\text{Hz}$ <sup>7</sup> and 4 kHz<sup>8</sup>), and the carbon nanotubes SC (636  $\text{Hz}$ <sup>37</sup>). The frequency at  $-45^\circ$  phase angle provides a characteristic time constant ( $1/f$ ), which is commonly adopted to evaluate the rate performance of the SC<sup>8,38</sup>. The characteristic time constants are 143 and 472  $\mu\text{s}$  for the SC based on the HCF (1.12  $\mu\text{m}$ ) and the HCF (1.83  $\mu\text{m}$ ) electrodes, respectively, indicating the HCF-based SC possesses ultrahigh-rate performance. At 120  $\text{Hz}$  (commonly used filtering frequency), the impedance phase angles of the HCF-based SCs are approximately  $-67^\circ$  and  $-64^\circ$  for the SC based on HCF (1.12  $\mu\text{m}$ ) and HCF (1.83  $\mu\text{m}$ ) electrodes, respectively, as compared with  $\sim 0^\circ$  for the activated carbon SC<sup>6</sup>,  $-15^\circ$  for the VOG-bridged coated nickel-foam SC<sup>7</sup>, and  $-82^\circ$  for the vertically oriented graphene SC<sup>6</sup>.

Energy density and power density of SC are quite important parameters for their real applications. To demonstrate the overall performance of the HCF-based SC, a Ragone plot is shown in Figure 7 comparing the performance of the HCF-based SCs with different energy storage devices, including the ( $\text{MnO}_2$ -PEDOT: PSS)/activated carbon (AC) SC<sup>39</sup>, the  $\text{MnO}_2/\text{AC}$  SC<sup>39</sup>, the laser scribing graphene (LSG) SC<sup>40</sup>, the nano-engineered carbon film (CNC) SC<sup>41</sup>, the 3 V/30 mF aluminum electrolytic capacitor and a 500  $\mu\text{Ah}$  lithium thin-film battery<sup>40</sup>. The volumetric energy density of the SC based on HCF (1.12  $\mu\text{m}$ ) ranges from 0.08 to 0.16  $\text{mWh}/\text{cm}^3$  (Figure 7a), which is lower than that of the  $\text{MnO}_2/\text{AC}$  SC<sup>39</sup>, comparable with the CNC film SC<sup>41</sup>, higher than that of the aqueous LSG SC<sup>40</sup>, and two-orders of magnitude higher than that of the aluminum electrolytic capacitor<sup>40</sup>. Furthermore, at energy density of 0.08  $\text{mWh}/\text{cm}^3$ , the SC can deliver a maximum power density of 1.49  $\text{W}/\text{cm}^3$ , which is 10 times higher than that of the  $\text{MnO}_2/\text{AC}$  SC<sup>39</sup> and the CNC film SC<sup>41</sup>, two-orders of magnitude higher than that of the 500- $\mu\text{Ah}$  thin-film lithium battery, comparable with the aqueous LSG SC, and close

to the lower end of the aluminum electrolytic capacitor<sup>40</sup>. These results indicate that the HCF-based SC possesses a high power density.

However, the energy density of the SC based on the HCF (1.12  $\mu\text{m}$ ) (Figure 7a and 7b) is lower than that of the carbon-based SCs reported by other groups<sup>42–46</sup>, which is because of lower loading mass/thickness in electrode. By increasing the carbon film thickness, the energy density can be significantly improved. For example, the maximum volumetric energy density increases from 0.16 to 0.40  $\text{mWh}/\text{cm}^3$  (Figure 7a), and the maximum gravimetric energy density increases from 0.32 to 0.79  $\text{Wh}/\text{kg}$  (Figure 7b) by increasing the carbon film thickness from 1.12 to 1.83  $\mu\text{m}$ , increasing more than two times. Furthermore, the maximum volumetric and gravimetric power densities of the SC based on HCF (1.83  $\mu\text{m}$ ) reach 3.10  $\text{W}/\text{cm}^3$  and 6.20  $\text{kW}/\text{kg}$ , respectively. We believe the performance can be further improved by increasing the thickness or the layer number of the carbon films.

## Discussion

The HCF with controllable thickness can be fabricated by a simple and scalable way. Understanding the growth mechanism of carbon films will be beneficial for regulating the thickness and structure of carbon films. In theory, the carbon content in Ni foil under different experimental conditions can be estimated. The diffusibility of carbon atom depends on its diffusivity  $D$  in Ni and the concentration on the surface of Ni (for in-diffusion) and in Ni (for out-diffusion and segregation)<sup>28–31,47</sup>. The diffusivity  $D$  of carbon atom in Ni at temperature  $T$  is expressed as<sup>28–30</sup>:

$$D = D_0 \exp(-E_D/k_B T) (\text{cm}^2/\text{s}), \quad (1)$$

where  $D_0$  is an entropic pre-factor,  $k_B$  is Boltzmann's constant, and  $E_D$  is the diffusion activation energy. Lander *et al.* found  $D_0 = 2.48 \text{ cm}^2/\text{s}$ ,  $E_D = 1.74 \text{ eV}$ <sup>28</sup>. The diffusion length of carbon atom in

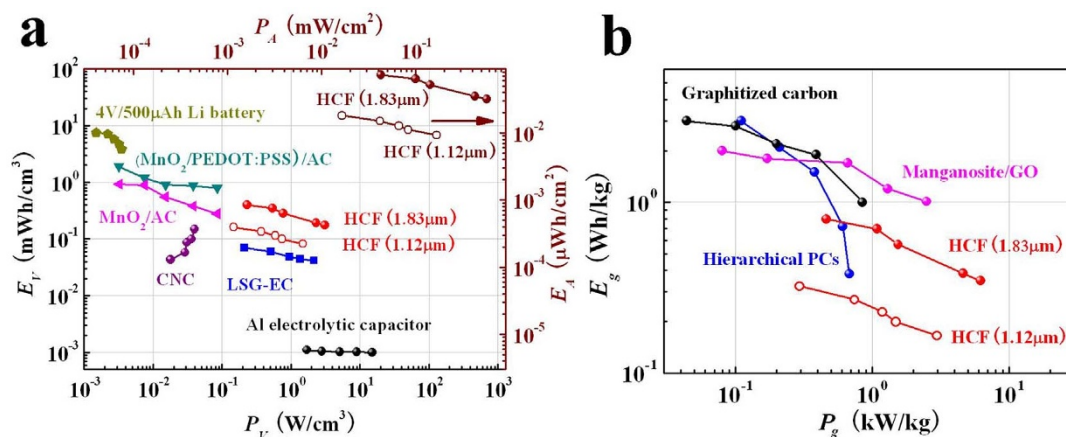


**Figure 7 | Ragone plots of HCF-based SC.** (a) Areal and volumetric energy densities versus power densities of the HCF-based SCs by using carbon films with different thicknesses compared with the (MnO<sub>2</sub>-PEDOT:PSS)/AC SC, the MnO<sub>2</sub>/AC SC<sup>39</sup>, the CNC SC<sup>41</sup>, the LSG SC, the aluminum electrolytic capacitors and a lithium thin-film battery<sup>40</sup>. (b) Gravimetric energy densities versus power densities of the HCF-based SCs compared with the manganosite/GO SC<sup>44</sup>, the graphitized carbon SC<sup>45</sup>, and the hierarchical porous carbon SC<sup>46</sup>.

Ni can be given by

$$L = 2(D\tau)^{1/2}(\text{cm}), \quad (2)$$

where  $\tau$  is diffusion time of carbon atom in Ni. It takes about one minute for carbon atom crossing the Ni foil (30  $\mu\text{m}$  thick) at 900°C, which is much smaller than the growth time used in this experiment (25 minutes). Therefore, a large number of carbon atoms dissolve into Ni foil during growth process (Figure 1b). According to Lander's<sup>28</sup> and Shelton's<sup>29</sup> theories, the solubility of carbon atom in Ni foil is given by

$$S = S_0 \exp(-E_p/k_B T)(\text{atoms}/\text{cm}^3), \quad (3)$$

where  $S_0$  is an entropic pre-factor, which depends on the concentration of carbon atom on the surface of Ni foil.  $E_p$  is the energy of precipitation. Lander *et al.*<sup>28</sup> found  $S_0 = 5.33 \times 10^{22}$  atoms/cm<sup>3</sup> and  $E_p = 0.42$  eV in the temperature range from 700 to 1300°C. Thus, the solubility of carbon atom in Ni foil can be calculated as about  $S = 8.10 \times 10^{20}$  atoms/cm<sup>3</sup> in our experiments (900°C). The volume of the Ni foil is 0.063 cm<sup>3</sup>, so the total number of carbon atom in the Ni foil is about  $N_T = 5.10 \times 10^{19}$  atoms. The thickness of the MGF is about 60 nm ( $\sim 176$  layers) (inset in Figure 4a). The graphene atomic layer density is about  $3.80 \times 10^{15}$  atoms/cm<sup>2</sup><sup>30</sup>. The area of the Ni foil is 21.0 cm<sup>2</sup>, so the total number of carbon atoms for two layers of MGF is  $N_g \approx 2 \times 21.0 \text{ cm}^2 \times 176 \times 3.8 \times 10^{15} \text{ atoms}/\text{cm}^2 = 2.81 \times 10^{19}$  atoms. Therefore, the total number of the trapped carbon atom in the Ni foil is  $N_r = N_T - N_g \approx 2.30 \times 10^{19}$  atoms, in other words, only part of the carbon atoms ( $\sim 55.1\%$ ) segregate/precipitate from Ni foil to form MGF. We estimate the total mass of the carbon atoms in Ni foil is about 0.46 mg. The mass of the PACF measured by an electronic balance after cleaning and drying is about  $(0.4 \pm 0.1)$  mg, which is smaller than 0.46 mg by the theoretical calculation because some of the carbon atoms are lost during corrosion process. The thickness of the PACF is about 1.00  $\mu\text{m}$  (inset in Figure 4c), and the area of the PACF is about  $5.4 \times 2.4 \text{ cm}^2$ . Therefore, the mass density of the PACF is about  $(0.3 \pm 0.1) \text{ g}/\text{cm}^3$ , which is far less than the density of graphite ( $2.23 \text{ g}/\text{cm}^3$ ). This result further confirms that the PACF has a porous structure. From equation (3), the solubility of carbon atom in Ni foil is strongly dependent on the growth temperature and flow ratio (CH<sub>4</sub>:H<sub>2</sub>). Therefore, the thickness of carbon films (including MGF and PACF) can be easily tuned by controlling both the growth temperature and the flow ratio (Figure 5a).

The sandwich-structured HCF can give full play to the advantages of high electrical conductivity of MGF and high specific surface area of PACF, and make it suitable to be used as an electrode material in

energy storage devices. The HCF-based SCs exhibit superior performance (including rate capability, frequency range, capacitance, and power density). The superior performance can be explained by the cooperative effects of the MGF, PACF, and geometric structure of device. First, the MGF and PACF possess high surface area, which is responsible for the high-charge storage capacity. Second, the porous structure of PACF is favorable for the rapid diffusion of ions by providing low-resistance channels. Third, the MGF has high electrical conductivity, which facilitates electron transport during the charge-discharge process. The geometric structure of electrodes is another important factor for generating high power SCs. The MGF and PACF in sandwich-structured HCF can be easily separated and has a loose interface (inset in Figure 2e), which provides a channel for electrolyte ion rapid penetration and transport.

In conclusion, we proposed and demonstrated for the first time a new way to fabricate large area free-standing sandwich-structured HCF composed of PACF and MGF by APCVD. This novel HCF inherits the advantages of graphene films and porous carbon materials thus exhibits good electrical conductivity, abundant porous structure, and excellent flexibility. The SCs based on sandwich-structured HCFs have high rate capability, wide frequency range for capacitive feature, a good capacitance performance, excellent cycle stability, and high power density. The performance of the HCF-based SC is significantly improved by increasing the thickness of the carbon films. Moreover, the PACF with a controllable thickness has transparent and porous characteristics, which enables many porous carbon film related applications as supports, hydrogen storage, catalysts, and air filters for substituting current porous carbon films. This reliable and scalable method also provides a general path for the fabrication of porous carbon materials and hybrid carbon materials with different structure forms by using different Ni substrates (such as foam Ni, Ni mesh, Ni wire, Ni cloth, etc.) and other metals with high carbon solubility. Therefore, this method can greatly expand the application scope of carbon materials.

## Methods

**Synthesis of HCF.** Ni foils (99.6% 30 and 40  $\mu\text{m}$  thick, Hefei Kejing Materials Technology Co.Ltd) were cut into  $7.0 \times 3.0 \text{ cm}^2$  slices and cleaned by dip in acetic acid: ethanol(1:1) for ten minutes and 7% hydrochloric acid ( $\geq 99.7\%$ , Sinopharm Chemical Reagent Co.Ltd), then rinsed by deionized water. The carbon films were grown by APCVD technique by using a hydrogen-methane mixed gas as carbon source (99.999%, Wuhan Minghui Gas Technology Co.Ltd). Before APCVD growth, the tube furnace was pumped to a base pressure of  $10^{-3}$  Torr followed by introduction of pure argon with the flow rate of 100 sccm for 10 min to create an inert atmosphere. The growth process can be described as follows four steps. First, the temperature raised from room temperature to 900°C in 30 min. The argon gas flowmeter was kept



constant (100 sccm) during the temperature rising process and closed when the temperature reached growth temperature (500~900°C). Second, the Ni foil was heat treated at growth temperature for 10 mins with the flow rate of 80 sccm hydrogen to improve Ni grain structure and remove surface oxides. Third, the methane gas (CH<sub>4</sub>) was introduced into reactor tube with the flow rate of 8 sccm (for low carbon concentration) or 80 sccm (for high carbon concentration). The flow ratio of the mixture gas was CH<sub>4</sub>:H<sub>2</sub> = 8:80 (or 80:8). The work pressure was controlled by a regulator valve. This procedure took about 25 min. Finally, the furnace was cooled down to 500°C by spontaneous cooling of the system (10°C/min) followed by rapidly cooling down to room temperature by opening the tube furnace. During cooling process, the mixed gas (CH<sub>4</sub> and H<sub>2</sub>) remained. To study the effect of the carbon film thickness on the performance of the HCF-based SC, a thicker HCF was fabricated by using thicker Ni foil (40 μm) at flow rate of CH<sub>4</sub>:H<sub>2</sub> = 8:80 and temperature of 900°C.

After the APCVD growth, the Ni foil was immersed into 0.5 mol/L ferric chloride solution. The MGF, PACF and HCF can be obtained by controlling the corrosion process. The MGF can be rapidly exfoliated from Ni foil in 2 minutes. After the exfoliation of the MGF, the Ni foil was placed in a freshly prepared ferric chloride solution. 5 hours later, the PACF appeared in the solution after the Ni foil entirely dissolved. The HCF can be obtained by completely dissolving of the Ni foil. The PACF, MGF and HCF were transferred by a silicon wafer into distilled water for several times to remove the residual ferric chloride. The PACF, MGF and HCF can be easily transferred to arbitrary substrates of interest.

**Characterization.** Crystal structures of the MGF and PACF were investigated by X-ray diffraction (XRD) on a D8 Advance powder X-ray diffractometer using Cu Kα radiation (λ = 0.15406 nm). The surface morphologies of the MGF and PACF were observed by a field-emission scanning electron microscope (SEM) (FEI Sirion 200). Surface element composition was investigated by energy dispersive spectroscopy (EDS) obtained on SEM. The microstructures of the MGF and PACF were characterized by transmission electron microscope (TEM) (FEI Tecnai G2-20) and selected area electron diffraction (SAED). The Raman spectra were obtained by HORIBA Jobin Yvon LabRAM Raman spectrometer. The thicknesses of the carbon films were measured by SEM. The electrical conductivity of the MGF, PACF, and HCFs were measured by RTS-8 four-probe (Guangzhou Science and Technology).

**Electrochemical Measurements.** The HCF was cut into two 2.0 × 3.0 cm<sup>2</sup> slices, which were used directly as electrodes for assembling symmetric supercapacitor with a cellulose separator (TF4030, NKK) in a 6 M KOH aqueous electrolyte solution. Electrochemical performances of the symmetric supercapacitors were tested by cyclic voltammetry, galvanostatic charge/discharge, and electrochemical impedance spectroscopy on a CHI 606B electrochemical analyzer system (Shanghai CHI Instruments Co.) under ambient conditions.

**Calculations.** The area specific capacitance value is calculated from the CV data according to the following equation:

$$C_{A-device} = \frac{1}{v\Delta U A} \int_{\Delta U} I(U)dU \quad (4)$$

Where  $v$  is the scan rate (V/s),  $\Delta U$  is the potential window (V),  $I(U)$  is the voltammetric discharge current (A), and  $A$  is the effective area (cm<sup>2</sup>), which is calculated based on the entire surface area of two electrodes. The area specific capacitance of one single electrode is calculated based on the effective area of the device according to the following formula:  $C = 4C_{A-device}$ . Where the factor 4 is related to normalization to the area of one electrode for the two identical capacitors in series<sup>48</sup>. The volumetric and areal specific capacitance values of devices are calculated from the galvanostatic curves at different current densities using the following equations:

$$C_{A-device} = \frac{I\Delta t}{\Delta U A}; \quad C_{V-device} = \frac{I\Delta t}{\Delta U V} \quad (5)$$

Where  $\Delta t/\Delta U$  is the slope of the discharge curve (V/s),  $A$  is the entire projected surface area of the device (cm<sup>2</sup>), and  $V$  is the effective volume of the electrode material (cm<sup>3</sup>). The Ragone plot is based on the volumetric and areal capacitance calculated from the discharge curves of GCD. The volumetric and areal energy density of the device are obtained from the formulae given by<sup>35</sup>

$$E_A = \frac{1}{2} \frac{C_{A-device} \Delta U^2}{3600}; \quad E_V = \frac{1}{2} \frac{C_{V-device} \Delta U^2}{3600} \quad (6)$$

where  $E_A$  and  $E_V$  are the areal and volumetric energy density (Wh/cm<sup>2</sup> and Wh/cm<sup>3</sup>), respectively,  $\Delta U$  is the discharge voltage (V). The volumetric and areal power density can be obtained from

$$P_A = 3600 \times E_A / \Delta t; \quad P_V = 3600 \times E_V / \Delta t \quad (7)$$

where  $P_A$  and  $P_V$  are the areal and volumetric power density (W/cm<sup>2</sup> and W/cm<sup>3</sup>), respectively, and  $\Delta t$  is the discharge time). The gravimetric energy density and power density of the SC can be obtained from

$$E_g = E_V / \rho; \quad P_g = P_V / \rho \quad (8)$$

where  $E_g$  and  $P_g$  are the gravimetric energy density (Wh/kg) and power density (W/kg), and  $\rho$  is total mass density of the HCF. It should be noted that the total

thicknesses of MGF and PACF were 120 and 1000 nm in the HCF (1.12 μm) electrode, respectively. Unit volume carbon film includes 10.7% MGF and 89.3% PACF. The mass densities of MGF and PACF are 2.23 and 0.3 g/cm<sup>3</sup>, respectively. Thus, mass density of the HCF (1.12 μm) is  $\rho = 10.7\% \times 2.23 \text{ g/cm}^3 + 89.3\% \times 0.3 \text{ g/cm}^3 \approx 0.5 \text{ g/cm}^3$ .

- Novoselov, K. S. *et al.* Electric field effect in atomically thin carbon films. *Science* **306**, 666–669 (2004).
- Zhang, Y., Tan, Y. W., Stormer, H. L. & Kim, P. Experimental Observation of Quantum Hall Effect and Berry's Phase in Graphene. *Nature* **438**, 201–204 (2005).
- Feng, D. *et al.* Free-Standing Mesoporous Carbon Thin Films with Highly Ordered Pore Architectures for Nanodevices. *J. Am. Chem. Soc.* **133**, 15148–56 (2011).
- Han, Y., Dong, X. T., Zhang, C. & Liu, S. X. Hierarchical porous carbon hollow-spheres as a high performance electrical double-layer capacitor material. *J. Power Sources* **211**, 92–96 (2012).
- Yoo, J. J. *et al.* Ultrathin Planar Graphene Supercapacitors. *Nano Lett.* **11**, 1423–1427 (2011).
- Miller, J. R., Outlaw, R. A. & Holloway, B. C. Graphene Double-Layer Capacitor with ac Line-Filtering Performance. *Science* **329**, 1637–1639 (2010).
- Bo, Z. *et al.* Vertically Oriented Graphene Bridging Active-Layer/Current-Collector Interface for Ultrahigh Rate Supercapacitors. *Adv. Mater.* **25**, 5799–5806 (2013).
- Ren, G. F., Pan, X., Bayne, S. & Fan, Z. Y. Kiloherzt ultrafast electrochemical supercapacitors based on perpendicularly-oriented graphene grown inside of nickel foam. *Carbon* **71**, 94–101 (2014).
- Zhao, X. C. *et al.* Synthesis and electrochemical performance of heteroatom-incorporated ordered mesoporous carbons. *Chem. Mater.* **22**, 5463–5473 (2010).
- Chmiola, J., Largeot, C., Taberna, P. L., Simon, P. & Gogotsi, Y. Monolithic carbide-derived carbon films for microsupercapacitors. *Science* **328**, 480–483 (2010).
- Jung N, Y. *et al.* Synthesis of Chemically Bonded Graphene/Carbon Nanotube Composites and their Application in Large Volumetric Capacitance Supercapacitors. *Adv. Mater.* **25**, 6854–6858 (2013).
- Luo, B., Liu, S. M. & Zhi, L. J. Chemical Approaches toward Graphene-Based Nanomaterials and their Applications in Energy-Related Areas. *Small* **8**, 630–646 (2012).
- Chen, H., Müller, M. B., Gilmore, K. J., Wallace, G. G. & Li, D. Mechanically Strong, Electrically Conductive, and Biocompatible Graphene Paper. *Adv. Mater.* **20**, 3557–3561 (2008).
- Wang, Q. *et al.* Two-dimensional mesoporous carbon sheet-like framework material for high-rate supercapacitors. *Carbon* **60**, 481–487 (2013).
- Yang, J., Chen, J. T., Yu, S. X., Yan, X. B. & Xue, Q. J. Synthesis of a graphene nanosheet film with attached amorphous carbon nanoparticles by their simultaneous electrodeposition. *Carbon* **48**, 2644–2673 (2010).
- Zhang, J. Y., Yu, Y. L. & Huang, D. M. Good electrical and mechanical properties induced by the multilayer graphene oxide sheets incorporated to amorphous carbon. *Solid State Sci.* **12**, 1183–1187 (2010).
- Li, X. *et al.* Hybrid thin films of graphene nanowhiskers and amorphous carbon as transparent conductors. *Chem. Commun.* **46**, 3502–3504 (2010).
- Li, X. *et al.* Large-Area Flexible Core-Shell Graphene/Porous Carbon Woven Fabric Films for Fiber Supercapacitor Electrodes. *Adv. Funct. Mater.* **23**, 4862–4869 (2013).
- Yang, X., Zhang, L., Zhang, F., Huang, Y. & Chen, Y. S. Sulfur-Infiltrated Graphene-Based Layered Porous Carbon Cathodes for High-Performance Lithium-Sulfur Batteries. *ACS Nano* **8**, 5208–5215, DOI: 10.1021/nn501284q (2014).
- Banerjee, A. N., Joo, S. W. & Min, B. K. Ambient-temperature fabrication of microporous carbon terminated with graphene walls by sputtering process for hydrogen storage applications. *Thin Solid Films* **537**, 49–57 (2013).
- Reina, A. *et al.* Large area, few-layer graphene films on arbitrary substrates by chemical vapor deposition. *Nano. Lett.* **9**, 30–35 (2009).
- Kim, K. S. *et al.* Large-scale pattern growth of graphene films for stretchable transparent electrodes. *Nature* **457**, 706–710 (2009).
- Yu, Q. K. *et al.* Graphene segregated on Ni surfaces and transferred to insulators. *Appl. Phys. Lett.* **93**, 113103 (2008).
- Chae, S. J. *et al.* Synthesis of Large-Area Graphene Layers on Poly-Nickel Substrate by Chemical Vapor Deposition: Wrinkle Formation. *Adv. Mater.* **21**, 2328–2333 (2009).
- Li, X. *et al.* Large-area synthesis of high-quality and uniform graphene films on copper foils. *Science* **324**, 1312–1314 (2009).
- Vijapur, S. H., Wang, D. & Botte, G. G. The growth of transparent amorphous carbon thin films from coal. *Carbon* **54**, 22–28 (2013).
- Cui, T. X. *et al.* Low-temperature synthesis of multilayer graphene/amorphous carbon hybrid films and their potential application in solar cells. *Nanoscale Res. Lett.* **7**, 453 (2012).
- Lander, J., Kern, H. & Beach, A. Solubility and Diffusion Coefficient of Carbon in Nickel: Reaction Rates of Nickel-Carbon Alloys with Barium Oxide. *J. Appl. Phys.* **23**, 1305–1309 (2004).
- Shelton, J. C., Patil, H. R. & Blakely, J. M. Equilibrium segregation of carbon to a nickel (111) surface: A surface phase transition. *Surf. Sci.* **43**, 493–520 (1974).



30. Baraton, L. *et al.* On the mechanisms of precipitation of graphene on nickel thin films. *EPL* **96**, 46003 (2011).
31. Eizenberg, M. & Blakely, J. M. Carbon monolayer phase condensation on Ni(III). *Surf. Sci.* **82**, 228–236 (1979).
32. Ferrari, A. C. *et al.* Raman spectrum of graphene and graphene layers. *Phys. Rev. Lett.* **97**, 187401 (2006).
33. Ferrari, A. C. & Robertson, J. Interpretation of Raman spectra of disordered and amorphous carbon. *Phys. Rev. B* **61**, 14095–14107 (2000).
34. Wang, D. W., Li, F., Wu, Z. S., Ren, W. & Cheng, H. M. Electrochemical interfacial capacitance in multilayer graphene sheets: Dependence on number of stacking layers. *Electrochem. Commun.* **11**, 1729–1732 (2009).
35. Conway, B. E. *Electrochemical Supercapacitors: Scientific Fundamentals and Technological Applications* Kluwer Academic/Plenum Publisher, New York 1999.
36. Sheng, K., Sun, Y., Li, C., Yuan, W. & Shi, G. Ultrahigh-rate, supercapacitors based on electrochemically reduced graphene oxide for ac line-filtering. *Sci. Rep.* **2**, 247; DOI: 10.1038/srep00247 (2012).
37. Du, C. & Pan, N. Supercapacitors using carbon nanotubes films by electrophoretic deposition. *J. Power Sources* **160**, 1487–1494 (2006).
38. Taberna, P. L., Simon, P. & Fauvarque, J. F. Electrochemical Characteristics and Impedance Spectroscopy Studies of Carbon-Carbon Supercapacitors. *J. Electrochem. Soc.* **150**, A292–A300 (2003).
39. Su, Z. J. *et al.* Co-electro-deposition of the MnO<sub>2</sub>-PEDOT: PSS nanostructured composite for high areal mass, flexible asymmetric supercapacitor devices. *J. Mater. Chem. A* **1**, 12432–12440 (2013).
40. El-Kady, M. F., Strong, V., Dubin, S. & Kaner, R. B. Laser Scribing of High-Performance and Flexible Graphene-Based Electrochemical Capacitors. *Science* **335**, 1326–1330 (2012).
41. Jung, H. Y., Karimi, M. B., Hahm, M. G., Ajayan, P. M. & Jung, Y. J. Transparent, flexible supercapacitors from nano-engineered carbon films. *Sci. Rep.* **2**, 773 (2012).
42. Sumboja, A., Foo, C. Y., Wang, X. & Lee, P. S. Large Areal Mass, Flexible and Free-Standing Reduced Graphene Oxide/Manganese Dioxide Paper for Asymmetric Supercapacitor Device. *Adv. Mater.* **25**, 2809–2815 (2013).
43. Kou, L. *et al.* Coaxial wet-spun yarn supercapacitors for high-energy density and safe wearable electronics. *Nat. Commun.* **5**, 3754 doi: 10.1038/ncomms4754 (2014).
44. Antiohos, D. *et al.* Manganosite-microwave exfoliated graphene oxide composites for asymmetric supercapacitor device applications. *Electrochimica Acta* **101**, 99–108 (2013).
45. Mun, Y. D. *et al.* Simple synthesis of hierarchically structured partially graphitized carbon by emulsion/blockcopolymer co-template method for high power supercapacitors. *Carbon* **64**, 391–402 (2013).
46. He, X. J. *et al.* Synthesis of hierarchical porous carbons for supercapacitors from coal tar pitch with nano-Fe<sub>2</sub>O<sub>3</sub> as template and activation agent coupled with KOH activation. *J. Mater. Chem. A* **1**, 9440–9448 (2013).
47. Losurdo, M., Giangregorio, M. M., Capezzuto, P. & Bruno, G. Graphene CVD growth on copper and nickel: role of hydrogen in kinetics and structure. *Phys. Chem. Chem. Phys.* **13**, 20836–20843 (2011).
48. Béguin, F., Presser, V., Balducci, A. & Frackowiak, E. Carbons and Electrolytes for Advanced Supercapacitors. *Adv. Mater.* **26**, 2219–2251 (2014).

## Acknowledgments

This work was supported by the NSAF (Grant No. U1230108) and the Fundamental Research Funds for the Central Universities (HUST: No. 2014NY010). We thank Analytical and Testing Center of Huazhong University of Science & Technology for all samples testing.

## Author contributions

H.W. proposed the project, analyzed data, and wrote the main manuscript text. S.W. and W.T. prepared the samples, measured the sheet resistances and electrochemical performance of the samples. D.Z. carried out the characterizations of the carbon films. Y.L. and L.Y. fabricated the carbon film samples. X.L. assisted electrochemical performance test. All authors reviewed the manuscript.

## Additional information

Supplementary information accompanies this paper at <http://www.nature.com/scientificreports>

Competing financial interests: The authors declare no competing financial interests.

How to cite this article: Wei, H. *et al.* Fabrication of thickness controllable free-standing sandwich-structured hybrid carbon film for high-rate and high-power supercapacitor. *Sci. Rep.* **4**, 7050; DOI:10.1038/srep07050 (2014).



This work is licensed under a Creative Commons Attribution-NonCommercial-ShareAlike 4.0 International License. The images or other third party material in this article are included in the article's Creative Commons license, unless indicated otherwise in the credit line; if the material is not included under the Creative Commons license, users will need to obtain permission from the license holder in order to reproduce the material. To view a copy of this license, visit <http://creativecommons.org/licenses/by-nc-sa/4.0/>